Advanced Materials

ADVANCED MATERIALS
www.advmat.de

RESEARCH ARTICLE

Green-Solvent-Grown Perovskite Single Crystals With Suppressed Defect Densities for Superior Photo- and X-Ray Detection

Tianqi Zhang[1] | Yaqi Hou[2] | Jinghui Han[3] | Depeng Chu[4] | Xiang Chen[1] | Guolong Chen[1] | Xiaotong Fan[1] | Xiao Yang[1] | Renzhu Zhang[1] | Yue Zhao[5] | Qingsen Zeng[5,6] | Yucheng Liu[4] | Shuli Wang[1,7] | Haotong Wei[3] | Zhong Chen[1,7] | Yue Lin[1,7] | Tae-Woo Lee[5,8]

[1]Fujian Engineering Research Center for Solid-State Lighting, Department of Electronic Science, School of Electronic Science and Engineering, Xiamen University, Xiamen, Fujian, China | [2]Institute of Flexible Electronics (IFE, Future Technologies), Xiang'an Campus, Xiamen University, Xiamen, Fujian, China | [3]State Key Laboratory of Supramolecular Structure and Materials, College of Chemistry, Jilin University, Changchun, Jilin, China | [4]Key Laboratory of Applied Surface and Colloid Chemistry, School of Materials Science and Engineering, National Ministry of Education, Shaanxi Normal University, Xi'an, China | [5]Department of Materials Science and Engineering, Seoul National University, Seoul, Republic of Korea | [6]Research Institute of Adv. Mater. (RIAM), Seoul National University, Seoul, Republic of Korea | [7]State Key Laboratory of Physical Chemistry of Solid Surface, Xiamen University, Xiamen, Fujian, China | [8]Institute of Engineering Research, Soft Foundry, Seoul National University, Seoul, Republic of Korea

Correspondence: Shuli Wang (slwang@xmu.edu.cn) | Haotong Wei (hweichem@jlu.edu.cn) | Yue Lin (yue.lin@xmu.edu.cn) | Tae-Woo Lee (twlees@snu.ac.kr)

Received: 6 January 2026 | **Revised:** 29 July 2026 | **Accepted:** 15 August 2026

Keywords: coordination theory | green-solvent | metal-halide perovskite single crystals | photodetector | steric hindrance | x-ray detector

ABSTRACT

Achieving environmentally sustainable synthesis of high-quality metal halide perovskite single crystals (MHP-SCs) is critical for advancing next-generation optoelectronic devices. The constrained solvent choices within the green chemistry framework pose a significant challenge to the fine control of crystallization pathways required for the growth of perfect MHP-SCs. Here, we introduce a new paradigm for crystallization control based on steric hindrance engineering using a quantitatively validated green solvent system with high GlaxoSmithKline green solvent scores. We demonstrate that the steric bulkiness of solvent molecules, rather than donor number alone, plays the dominant role in governing the coordination strength between Pb^{2+} and solvent, thereby regulating precursor complex stability and crystallization kinetics. Finely tuned steric environments promote the unprecedented fast growth of $MAPbI_3$ SCs with a record-low trap density (2.56×10^8 cm^{-3}) and narrowest x-ray diffraction linewidth of 0.00802° (28.9″). These defect-suppressed $MAPbI_3$ SCs enable photodetectors with an ultrahigh specific detectivity of 6.8×10^{13} Jones and x-ray detectors with a low detection limit of 3.6 nGy_{air} s^{-1}. The steric hindrance engineering strategy proves universal across perovskite compositions. This work establishes a sustainable, scalable platform for the growth of high-quality MHP-SCs using quantitatively green solvents.

1 | Introduction

Metal halide perovskite single crystals (MHP-SCs) have emerged as promising materials for next-generation optoelectronic devices, including photovoltaics [1, 2], light-emitting diodes [3, 4], photodetectors [5, 6], and x-ray detectors [7, 8]. Their exceptional optoelectronic properties, particularly when combined with high crystalline quality and low trap densities, are key to achieving

Tianqi Zhang, Yaqi Hou, and Jinghui Han contributed equally to this work.

superior device performance [8]. Among various growth techniques, inverse temperature crystallization (ITC) has gained attention as a fast, low-temperature, solution-based method that offers high reproducibility [9]. However, conventional ITC for the synthesis of perovskite single crystals faces inherent challenges: (i) use of non-green solvents such as γ-butyrolactone (GBL), *N*,*N*-dimethylformamide (DMF), and dimethylsulfoxide (DMSO) [10, 11], and (ii) limited single crystal quality due to lacking of precise crystallization control. Specifically, the as-grown SCs often still show insufficient control over surface morphology, as reflected by high surface roughness, along with limited local structural homogeneity and poorly controlled crystallization kinetics [12–14].

The adoption of green chemistry principles further restricts the choice of solvents, narrowing the processing window, mainly originates from two aspects: the limited availability of green solvents and their constrained physicochemical parameter space. Compared with conventional solvents (e.g., DMF, DMSO, GBL), green solvents suitable for perovskite processing are relatively limited in both number and physicochemical diversity, typically exhibiting (i) a narrower range of dielectric constants and donor numbers, or (ii) weaker coordination ability toward Pb^{2+}. In addition, the structural diversity of green solvents is limited, making it difficult to effectively implement solvent-mixing strategies or donor-number engineering, thereby further restricting the expansion of the processing window [15, 16]. As a result, obtaining high-quality MHP-SCs with low defect densities remains a significant challenge in the framework of green chemistry. This difficulty becomes more pronounced for crystals with mixed A-sites or halides, as even non-green solvent syntheses frequently yield MHP-SCs with high defect densities [11, 17]. Therefore, there is an urgent need for an ITC-compatible green solvent system that not only meets stringent environmental standards but also enables precise crystallization control across a wide range of MHP compositions to achieve low-defect single crystals essential for the development of high-performance optoelectronic devices.

In this work, we introduce a new crystallization-control paradigm for the growth of perovskite single crystals with low defect densities: steric hindrance engineering. This approach is implemented within a quantitatively validated green solvent system using low-toxicity lactone solvents, δ-valerolactone (DVL) and γ-caprolactone (GCL). DVL and GCL possess distinct molecular steric profiles but similar donor numbers (DN) and closely matched boiling points. Adjusting the volume ratio of the two solvents tunes the mean steric hindrance of the solvent environment without introducing volatility imbalance. It is demonstrated that this steric control, independent of DN, governs Pb^{2+}-solvent coordination strength and thus dictates crystallization kinetics (Figure 1a). This approach enables unprecedentedly fast and reproducible growth of $MAPbI_3$ SCs with record-low trap densities (2.56×10^8 cm^{-3}) and the narrowest x-ray diffraction (XRD) rocking curve linewidth reported to date (0.00720). These defect-suppressed crystals deliver photodetectors with ultra-high specific detectivity and x-ray detectors with sub-medical-threshold detection limits. Furthermore, the steric hindrance strategy proves general across multiple MHP compositions, offering a sustainable and scalable route to high-performance MHP-SCs.

2 | Results

2.1 | Steric Hindrance Effect on ITC Growth of MHP-SCs

The ITC crystallization proceeds through sequential formation-dissociation of Pb^{2+}-solvent complexes followed by assembly of Pb^{2+}-halide octahedra, with kinetics primarily governed by A-site cations (e.g., Cs^+, MA^+, FA^+) [9, 18], and Pb^{2+}-solvent coordination strength (Figures S1 and S2). Therefore, the solvent plays a critical role in the ITC process—only those with suitable coordination capability and molecular structure can facilitate efficient crystallization (Figures S3 and S4). In single-solvent systems, fixed coordination strength necessitates adjusting the growth temperature for different A-site cations, creating a trade-off between crystal quality and precursor utilization. Although mixed-solvent systems with divergent DN provide greater adaptability, their boiling-point mismatch (Figure S5) often compromises crystal quality and reproducibility (Figure S6).

To address these challenges, we employed DVL and GCL, two bio-derived, low-toxicity lactone solvents which are selected for their high GlaxoSmithKline (GSK) sustainability scores (both larger than 7, Tables S3 and S4) [19–22]. These solvents are bio-based and environmentally benign while possessing favorable physicochemical properties, such as low vapor pressure and high boiling points, which reduce health and environmental risks. While DVL and GCL share closely matched DNs and boiling points, they differ significantly in molecular geometry and steric hindrance (Figure 1a). In this work, "steric hindrance" is defined as the geometric exclusion effect arising from the molecular size and conformational constraints of solvent molecules within the first solvation shell of Pb^{2+}, which limits the accessibility, number, and packing compactness of coordinating donor atoms around Pb^{2+}. This effect is treated as a geometric-statistical constraint that is distinct from, but complementary to, electronic descriptors such as donor number and polarity.

Despite their similar Lewis basicities (Table S3), it is observed in our experiment that these steric differences lead to distinct Pb^{2+}-solvent coordination behaviors: the smaller DVL molecules bind more strongly to Pb^{2+}, forming stable Pb^{2+}-DVL complexes (Figure 1b). Conversely, the larger GCL molecules form weaker, looser Pb^{2+}-GCL complexes (Figure 1c). This difference in bonding strength means Pb^{2+}-DVL complexes dissociate at higher temperatures than Pb^{2+}-GCL complexes. This leads to rapid growth of large, but highly-defected MHP-SCs with DVL, while GCL's lower dissociation temperature results in a proliferation of less-defected micro-crystals.

The pronounced differences in crystallization behaviors of DVL and GCL, together with their mutual miscibility, motivated us to fine-tune crystallization kinetics by mixing these solvents in varying volume ratios. As illustrated in Figure 1d, dissolving MHP precursors in a DVL-GCL mixture results in the formation of hybrid-coordinated complexes containing both solvents. The coordination strength of these hybrid complexes lies between that of Pb^{2+}-DVL and Pb^{2+}-GCL complexes and can be systematically adjusted by changing DVL-to-GCL ratio. By controlling the solvent ratio, we can precisely modulate the

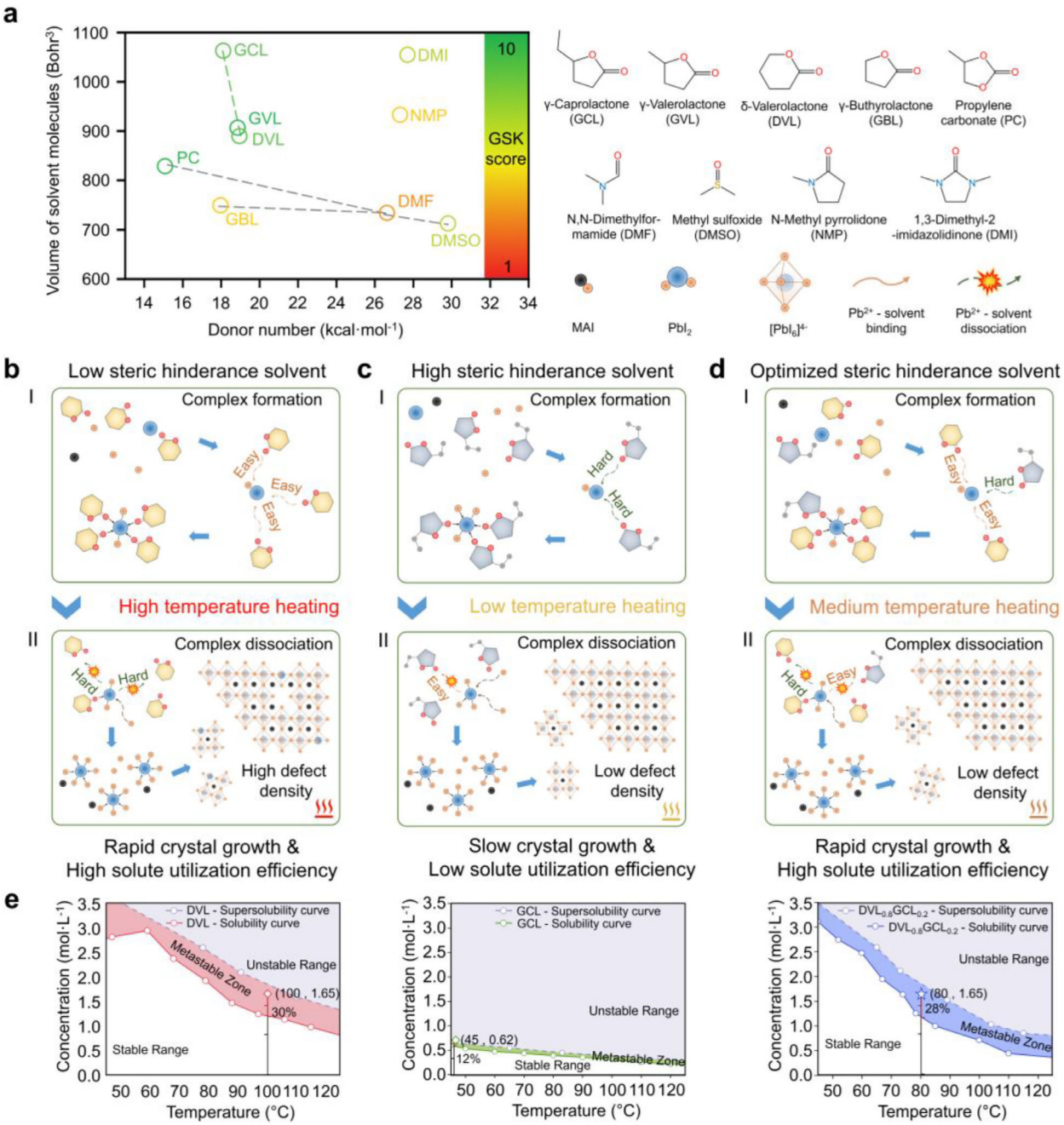

FIGURE 1 | Steric hindrance engineering strategy for ITC growth of MHP-SCs. (a) Left: Volume of solvent molecules versus DN (Table S3). Solvent data points are color-coded by GSK scores, with a green-to-red gradient indicating high-to-low scores (Table S4). Gray and green dashed lines denote solvent selection strategies based on DN and steric hindrance engineering, respectively. Right: legends of (b–d) Crystallization kinetics of solvents with different steric hindrances. (b) Low steric hindrance (DVL): DVL forms strongly bonded Pb^{2+}-DVL complexes requiring high dissociation temperatures, resulting in rapid yet defect-rich growth. (c) High steric hindrance (GCL): Weakly bound Pb^{2+}-GCL complexes dissociate at low temperatures, permitting defect-suppressed but slow microcrystal growth. (d) Sterically optimized mixed solvent ($DVL_{0.8}GCL_{0.2}$): Balanced DVL/GCL mixture yields moderate-bonding Pb^{2+} complexes. Intermediate dissociation temperatures enable fast growth of large, low-defect crystals. (e) Tunable solubility profiles in (i) low, (ii) high, and (iii) optimized steric environments, where increasing steric hindrance narrows and shifts the metastable zone downward. An optimized steric environment enables efficient precursor utilization at low growth temperatures.

mean steric environment of the mixed solvent, thereby tuning the Pb^{2+}-solvent coordination affinity to an optimal range that promotes dissociation at moderate temperatures. Under these conditions, low-defect-density MHP-SCs can be rapidly grown. This modulation of Pb^{2+}-solvent interactions is macroscopically reflected as a shift of the metastable zone in the solubility–supersolubility diagram (Figures 1e and S2). Increasing the mean steric hindrance moves this zone toward lower temperatures and smaller solute concentrations, allowing the growth point to be positioned in an optimized region that simultaneously reduces crystallization temperature and maintains high solute utilization and growth rates.

2.2 | Theoretical and Experimental Validations

To demonstrate the hypothesis of steric effect on crystallization within the ITC method, we selected $MAPbI_3$ SC as a representative MHP-SC. These crystals were grown in three green solvents respectively, DVL, γ-valerolactone (GVL), and GCL. These lactones were chosen due to their homologous molecular structures, similar DNs, and comparable boiling points, while exhibiting progressively increasing molecular volumes (Table S3). Further details on our solvent selection criteria are provided in Supporting Notes 2 and 3 (Figures S3 and S4).

Evidence contradicting classical Lewis theory emerged from surface electrostatic potentials (ESP) calculated by density functional theory (DFT) (Figure 2a), providing a robust thermodynamic basis for understanding Pb^{2+}-solvent coordination. As expected, Pb^{2+} ions preferentially bind near the negatively charged carbonyl oxygen sites of the solvent molecules. Interestingly, the binding energy of Pb^{2+}-GCL (−5.6471 eV) was higher than that of Pb^{2+}-GVL (−5.5591 eV), contradicting the experimental observation that precursor solubility is lower in GCL than in GVL (Table S2). This discrepancy suggests the involvement of additional factors in Pb^{2+}-solvent coordination–dissociation. Indeed, the molecular volumes of DVL, GVL, and GCL, estimated from van der Waals surface enclosures (Table S5), displayed a negative correlation with precursor solubility, highlighting the substantial role of steric effects.

To probe this, we performed ab initio molecular dynamics (AIMD) simulations. Figure 2b,c show representative solvent distributions around Pb^{2+} and the corresponding radial distribution functions of O atoms in solvent molecules around Pb^{2+} $g_{Pb\text{-}O}(r)$. The results indicate that three solvent molecules form two coordination layers around Pb^{2+}, with a denser inner layer supported by the higher first peak in $g_{Pb\text{-}O}(r)$ (2–3 Å) compared to the second peak (4–5 Å). By integrating $g_{Pb\text{-}O}(r)$ to the first minimum, we obtained coordination numbers following the order: DVL (9.89) > GVL (8.57) > GCL (7.97). This trend reflects the varied crystallization kinetics observed experimentally: lower coordination numbers correspond to greater steric hindrance, weaker Pb^{2+}-solvent binding, and looser complexes. Accordingly, GCL exhibits the highest steric hindrance and the weakest Pb^{2+}-solvent coordination, while DVL shows the lowest steric hindrance and the strongest coordination affinity. Further details of these DFT calculations are provided in Supporting Note 1.

To quantitatively evaluate steric effects, we introduced the buried volume descriptor ($\%V_b$) based on an idealized Pb^{2+}-solvent coordination geometry (Figure S7). The calculated $\%V_b$ values for GCL, DVL, and GVL are 58.4%, 55.1%, and 54.6%, respectively, indicating that GCL creates the most sterically congested local coordination environment among the three solvents. However, because $\%V_b$ is derived from an idealized static coordination geometry, it is used here as a complementary descriptor rather than a standalone predictor of coordination strength. The dynamic AIMD results, particularly the coordination numbers derived from the radial distribution functions, provide a more realistic description of solvent accessibility and coordination exchange in solution.

The outcomes of AIMD simulations align with experimental findings. $[PbI_n]S_{6-n}^{2-n}$ (S: solvent) complexes, exhibiting varying n values, exhibit distinct UV absorption peaks at 325, 370, and 426 nm, corresponding to $[PbI_2]S_4$, $[PbI_3]S^{3-}$, and $[PbI_4]S_2^{2-}$, respectively (Figure 2d). For DVL and GVL, the predominant complexes are $[PbI_2]S_4$ and $[PbI_3]S_3^-$, with stronger peak intensities for DVL-Pb^{2+} compared to Pb^{2+}-GVL, indicating higher coordination affinity of DVL toward Pb^{2+}. In contrast, GCL primarily forms $[PbI_3]S_{3-}$ and $[PbI_4]S_2^{2-}$ complexes, with the weakest peak intensities relative to DVL and GVL, and no $[PbI_2]S_4$ peak is observed. This suggests significant steric hindrance in GCL, resulting in the weakest Pb^{2+} coordination. Additionally, in situ UV absorption spectra demonstrate DVL's superior coordination affinity over GCL, evidenced by immediate emergence of $[PbI_2]S_4$ peak and rise of the $[PbI_3]S_{3-}$ peak upon DVL addition to a GCL-Pb^{2+} solution (Figure S8).

To further confirm the affinity between Pb^{2+} and lactones with different steric hindrances, we employed nuclear magnetic resonance (NMR) and Fourier transform infrared (FTIR) spectroscopy measurements. In the ^{207}Pb NMR spectra, the Pb^{2+} peak shifts downfield from 1423 ppm (the peak in solid-state NMR [23]) to 1583, 1553, and 1509 ppm for DVL, GVL, and GCL, respectively (Figures 2e and S9). This indicates varying degrees of I^- replacement by C═O, thus reflecting a reduction in Pb^{2+} affinity for these solvents. Due to the fact that the Pb^{2+} binds to the carbonyl oxygen, the degree of broadening in the C═O peak in FTIR spectra positively correlates with the coordination strength of the solvent molecule to Pb^{2+}. Notably, the most significant broadening was observed in DVL, and the least in GCL, which further validates the hypothesis that coordination affinity diminishes with increasing steric hindrance (Figure 2f). Interestingly, FTIR spectra of the precursor dissolved in a mixed solvent of DVL and GCL show a combination of individual peaks from pure DVL and GCL, with their relative intensity positively correlating with the volume ratio of the two solvents (Figures 2f and S10). This suggests that the mean coordination affinity of the mixed solvent lies between those of pure DVL and GCL and can be continuously adjusted by varying the volume ratio. Consequently, this mixed solvent system can serve as a powerful platform for investigating steric hindrance engineering in the ITC growth of MHP-SCs. In summary, the $\%V_b$ analysis, together with MD/AIMD simulations and multiple experimental characterizations, consistently indicates that steric hindrance is an important factor in modulating the Pb^{2+}-solvent coordination strength and, together with solvation effects, governs the crystallization behavior.

2.3 | Steric Hindrance Engineering of Mixed Solvent System

Based on the steric regulation of Pb^{2+}-solvent coordination strength, we developed a solvent-engineering strategy for MHP-SC growth. $MAPbI_3$ SCs were grown using mixed DVL/GCL solvents with varying ratios (0.1 increment) to identify the optimal composition (Figure S11), and the screening of growth conditions is detailed in the Supporting Note 4.

We observed that the steric hindrance of the mixed solvent, quantified by the weighted average molecular volume, increased with

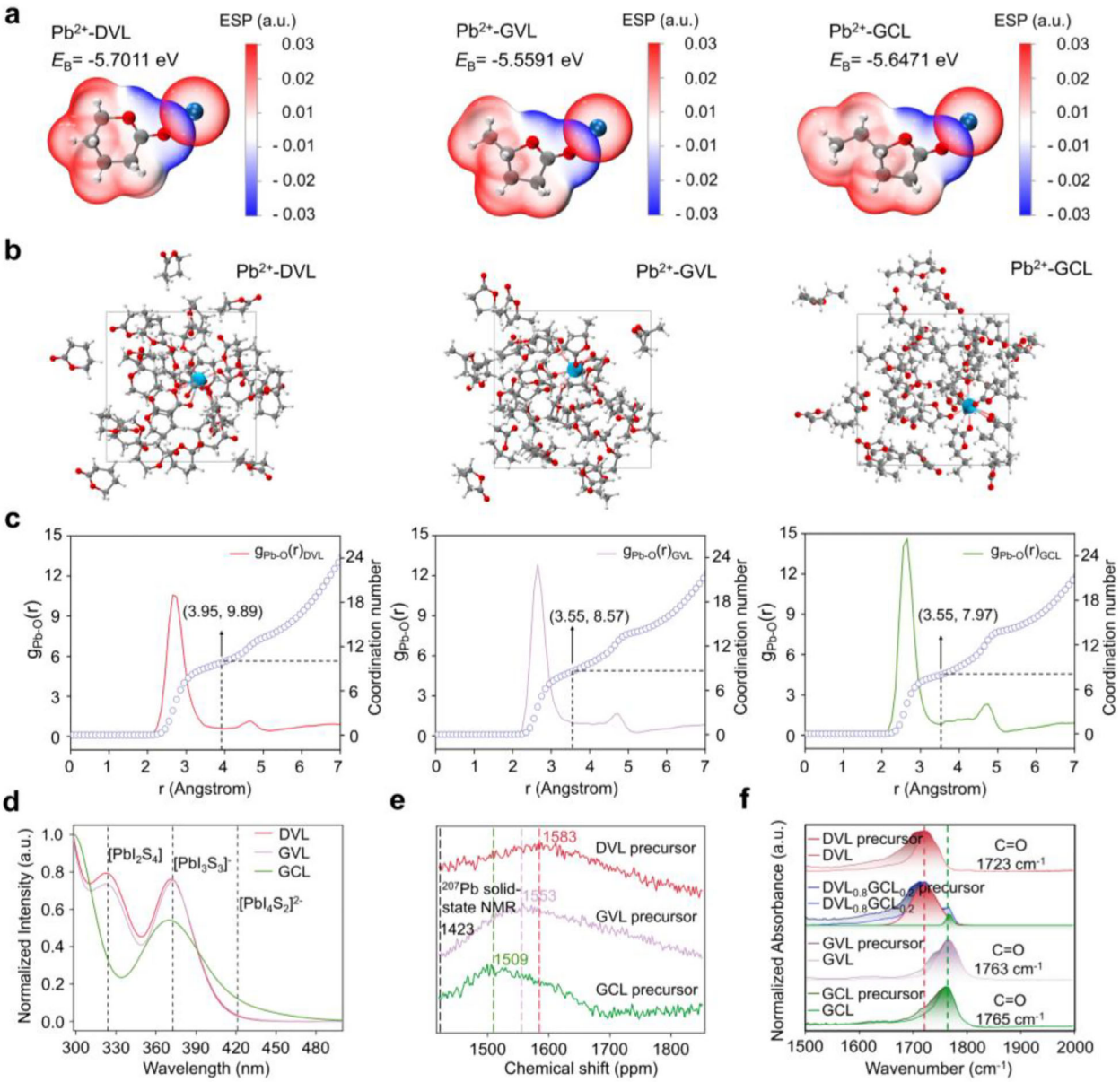

FIGURE 2 | Theoretical and experimental demonstrations of steric effect on coordination affinity between Pb^{2+} and solvent. (a) Molecular electrostatic potential of DVL, GVL, GCL, along with calculated binding energy (E_B) between Pb^{2+} and each solvent molecule. (b) AIMD simulation showing spatial distribution of Pb^{2+} ions in DVL, GVL, and GCL. (c) Radial distribution functions $g_{Pb\text{-}O}(r)$ and coordination numbers of O atoms around Pb^{2+} ions in the three solvents. (d) UV–vis absorption spectra of Pb-based precursor solutions in DVL, GVL, and GCL, revealing differences in complex formation. (e) Zoomed-in ^{207}Pb NMR spectra of precursor solutions in DVL, GVL, and GCL (full spectra provided in Figure S8), indicating variations in local chemical environments around Pb^{2+} ions. (f) FTIR spectra of precursor solutions in DVL, GVL, GCL, the mixed solvent $DVL_{0.8}GCL_{0.2}$ and corresponding pure solvents, showing vibrational signatures related to Pb^{2+}-solvent interactions.

increasing GCL content, whereas both the growth temperature (T_G) and crystal growth rate decreased (Figure S12 and Table S7). At relatively high DVL contents, the resulting crystals displayed well-defined morphologies, whereas other compositions with higher GCL fractions yielded only micron-sized crystallites (Figure 3a, inset). This result suggests that a highly sterically hindered solvent environment suppresses heterogeneous seed growth while promoting homogeneous nucleation, leading to the formation of microcrystals. A comprehensive comparison of crystals grown in different solvent systems was performed in terms of growth rate, surface roughness, growth temperature, and defect density (Figures S12–S14). The results show that although $MAPbI_3$ SCs grown in $DVL_{0.8}GCL_{0.2}$ exhibit a slightly slower growth rate than those grown in pure DVL, the growth temperature is substantially reduced from 115°C to 80°C (Table S7). The $DVL_{0.8}GCL_{0.2}$ composition was therefore selected because it provides the best balance between rapid crystal growth and defect suppression, rather than because it maximized every individual parameter.

To elucidate how the steric environment of solvents influences microcrystal (seed) formation, we systematically optimized the DVL-GCL solvent ratio for $MAPbI_3$ SC growth. Transmission electron microscopy (TEM) analysis of dried precursor solutions

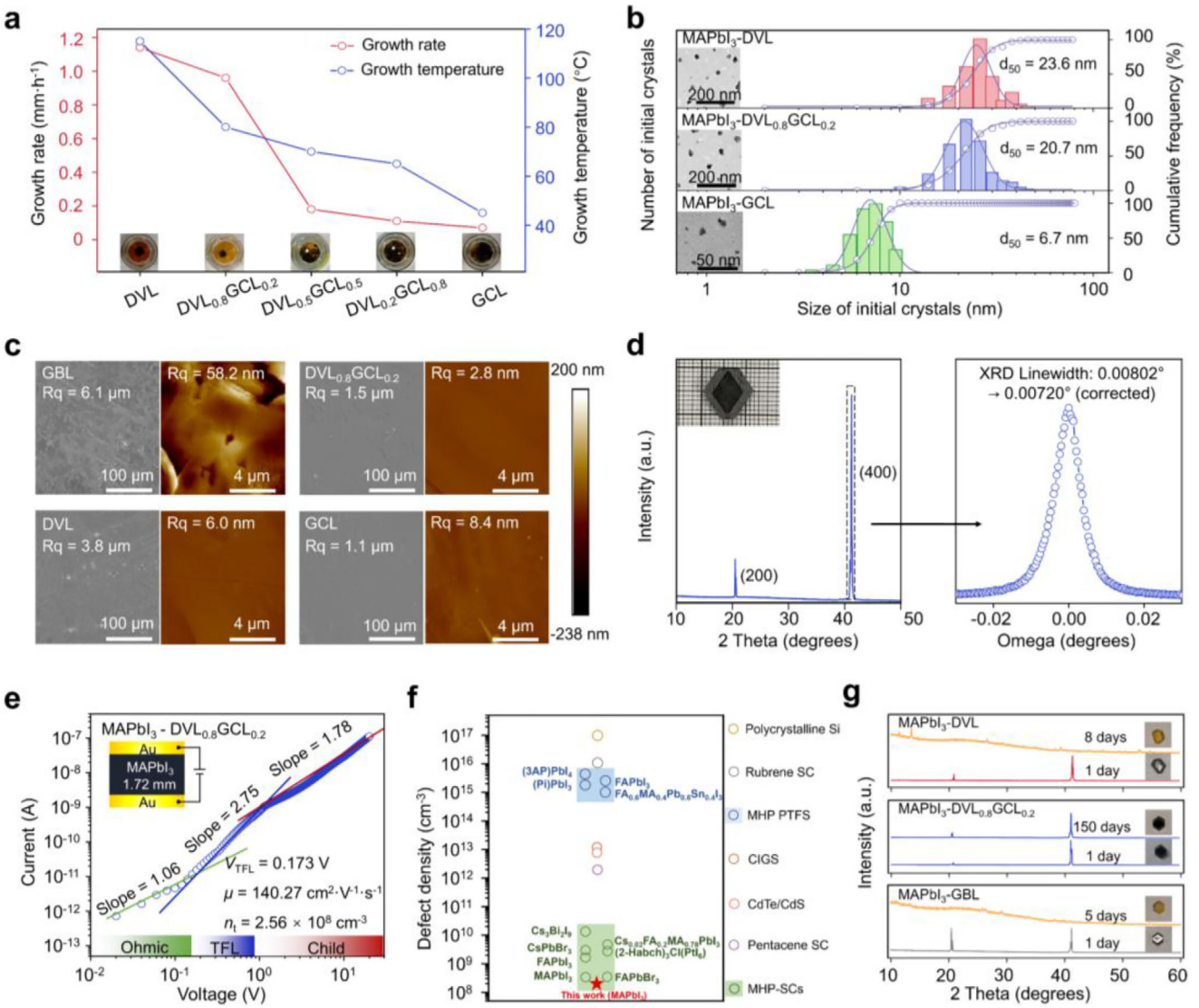

FIGURE 3 | Characterizations of $MAPbI_3$ SCs grown using a steric-hindrance-regulated DVL-GCL mixed solvent system. (a) Crystal growth rate and corresponding T_G profiles for $MAPbI_3$ SCs grown in DVL, GCL, and DVL-GCL mixtures with varying volume ratios. (b) TEM images and size distributions of $MAPbI_3$ microcrystals in precursor solution grown in DVL, GCL, and the optimized mixed solvent $DVL_{0.8}GCL_{0.2}$, highlighting differences in crystal size and morphology. (c) Surface morphology characterization by laser confocal microscopy (gray scale) and atomic force microscopy (yellow tone) for $MAPbI_3$-GBL, $MAPbI_3$-DVL, $MAPbI_3$-GCL, and $MAPbI_3$-$DVL_{0.8}GCL_{0.2}$. (d) Left: XRD pattern of $MAPbI_3$-$DVL_{0.8}GCL_{0.2}$; right: rocking curve of the (400) reflection; inset shows the crystal sample under XRD testing, the corrected linewidth is 0.00720° after instrumental broadening subtraction. (e) Dark *I–V* characteristics of $MAPbI_3$-$DVL_{0.8}GCL_{0.2}$ (see Supporting Note 4); inset: schematic of the tested device and key parameters. (f) Comparison of trap density of $MAPbI_3$-$DVL_{0.8}GCL_{0.2}$ with reported values for typical halide perovskites and commercial semiconductors (data summarized in Table S9), demonstrating the exceptional crystal quality achieved in this work. (g) XRD spectra of $MAPbI_3$-DVL, $MAPbI_3$-$DVL_{0.8}GCL_{0.2}$, and $MAPbI_3$-GBL over time at ambient storage. Full evolutions are illustrated in Figure S24.

revealed that the average nanoscale crystallite size (d_{50}) decreased from 23.6 nm to 6.7 nm as the mean steric hindrance increased (Figure 3b). Representative TEM images of larger areas from three precursor samples are shown in Figure S15. Notably, the $DVL_{0.8}GCL_{0.2}$ composition produced microcrystals comparable in size to those obtained with pure DVL, a feature known to facilitate subsequent MHP-SC growth [10]. A similar trend in colloidal microcrystal size was confirmed by dynamic light scattering (DLS) measurements (Figure S16). The reduction in microcrystal size under higher steric hindrance conditions promotes the formation of $[PbI_x]^{2-x}$ complexes with higher x values [24, 25], weaker Pb^{2+}-solvent coordination in more sterically hindered solvent environments. In the following text, samples grown in different solvents are denoted as "MHP-solvent."

After determining the optimal solvent ratio for $MAPbI_3$ SC growth, we compared the performance of crystals synthesized in various solvents. MHP-SCs grown in GBL were included as a control, as GBL remains the most widely used solvent for $MAPbI_3$ SC crystallization. The surface morphology and roughness of the as-grown $MAPbI_3$ SCs were analyzed using a multi-scale approach combining laser confocal microscopy (micrometer-scale) and atomic force microscopy (AFM, nanometer-scale). As depicted in Figures 3c and S13, $MAPbI_3$ SCs grown in solvents

with low steric hindrance (GBL and DVL, see Figure 1a) exhibited uneven surfaces at the micron-scale, with root mean square (R_q) roughness values of 6.1 and 3.8 μm. In contrast, $MAPbI_3$-$DVL_{0.8}GCL_{0.2}$, with its slightly increased mean steric hindrance, showed a R_q of 1.47 μm, comparable to the flattest $MAPbI_3$-GCL (1.05 μm) grown in GCL, which possesses the highest steric hindrance. At the nanoscale, the R_q of $MAPbI_3$-$DVL_{0.8}GCL_{0.2}$ was 2.8 nm, the lowest among the four samples and, notably, even lower than that of $MAPbI_3$-GCL (Figures 3c and S17).

XRD spectra confirmed the excellent crystal structure of $MAPbI_3$-$DVL_{0.8}GCL_{0.2}$, with two characteristic peaks at 20.57° and 41.19° corresponding to the (200) and (400) crystallographic planes, respectively (Figure 3d left). A detailed examination of the (400) peak using XRD rocking curve analysis (Figure 3d right) revealed a linewidth of 0.00802°. After deconvolution of instrumental broadening, the intrinsic linewidth is determined to be 0.00720° (Figure S18). This significantly outperforms the previously reported lowest value of 0.01° (36″) for $MAPbI_3$ SCs grown in GBL [26]. Such high crystallinity reduces lattice scattering, thereby enhancing carrier mobility and charge collection efficiency [27]. These characteristics in the crystalline structure indicate that $MAPbI_3$-$DVL_{0.8}GCL_{0.2}$ possesses the least defective structure compared with crystals grown with other volume ratios.

The quality of MHP-SCs can also be assessed through their electrical properties. Figures 3e and S19a–d present the forward-bias dark current–voltage (*I–V*) curves of $MAPbI_3$ SCs grown in various solvents. Crystal defects trap carriers and induce non-radiative recombination, thereby reducing photoelectric conversion efficiency. In addition, defect-induced ion migration increases dark current and causes current drift. MHP-SCs with low trap densities (n_t) effectively suppress carrier recombination and consequently prolong carrier lifetimes [27, 28]. The n_t of $MAPbI_3$-$DVL_{0.8}GCL_{0.2}$ determined by the space-charge-limited current (SCLC) method, was 2.56×10^8 cm^{-3}, a remarkably low value, lower than any previously reported for $MAPbI_3$ SC and among the lowest for MHP-SCs overall [29–35]. Notably, consistent results were obtained across multiple independently grown crystals, all exhibiting similarly low trap densities, confirming the reproducibility and reliability of this observation (Figure S20). This value is also 7–11 orders of magnitude lower than that of perovskite polycrystalline thin films (PTFs) (10^{15}–10^{19} cm^{-3}) [36–39]. Moreover, it surpasses commercials semiconductors, including polycrystalline silicon (10^{13}–10^{14} cm^{-3}) [13], copper indium gallium selenide (CIGS, (≈10^{13} cm^{-3}) [40], CdTe/CdS (10^{11}–10^{13} cm^{-3}) [41], and organic semiconductors such as rubrene SCs (≈10^{16} cm^{-3}) and pentacene SCs (10^{14}–10^{15} cm^{-3}) (Figures 3f and Table S9) [42].

Deep-level transient spectroscopy (DLTS) was used to analyze trap energy levels and defect densities [43]. Current-mode DLTS (*I*-DLTS) is independent of doping concentration and only requires sufficient free carriers for trap filling, making it suitable for high-resistivity SCs [44]. Arrhenius analysis based on DLTS peaks (Figure S22) revealed multiple deep-level defects distributed between approximately 0.10 eV and 0.57 eV, with defect densities on the order of 10^{10} cm^{-3} and capture cross-sections of 10^{-} [12]-10^{-} [18] cm^2 (Table S8). These results are consistent in order of magnitude with the trap densities obtained from SCLC analysis. The discrepancy in absolute values can be attributed to their different sensitivities: SCLC mainly probes shallow and transport-related traps, whereas DLTS is more sensitive to thermally activated deep-level defects. Notably, no dominant high-density trap center was observed in the DLTS spectra, indicating a dispersed defect distribution and further confirming the low defect concentration and high crystalline quality of the SCs. We further employed thermal admittance spectroscopy to analyze the trap density of states (tDOS). The resulting tDOS spectra (Figure S23) revealed two distinct trap regions: shallow traps (Region I, $E_\omega \approx 0.23$ eV), mainly associated with bulk defects, and deep traps (Region II, $E_\omega > 0.40$ eV), typically attributed to surface or interfacial defects. Comparison among different solvent systems showed that GVL-based single crystals exhibit the highest tDOS, followed by DVL, while the $DVL_{0.8}GCL_{0.2}$ sample consistently showed the lowest values across the entire energy range. The shallow trap density was reduced by ∼5 times, and the deep trap density decreased by nearly one order of magnitude, indicating effective defect suppression. These results are consistent with DLTS and SCLC analyses in terms of both energy distribution and magnitude, further confirming that the $DVL_{0.8}GCL_{0.2}$ solvent system exhibits superior defect suppression capability.

The mobility-lifetime product of $MAPbI_3$-$DVL_{0.8}GCL_{0.2}$, extracted from the photocurrent curves in Figure S19e, was 1.4×10^{-3} cm^2 V^{-1} s^{-1}. This value is higher than that of SCs grown in mixed solvents with other ratios and pure solvents, indicating a uniform crystalline structure yielded by $DVL_{0.8}GCL_{0.2}$. The extracted mobilities show an overall negative correlation with trap densities (Figure S21), confirming that defect suppression is the primary factor influencing the carrier transport, rather than fitting artifacts. The dark *I–V* curve of $MAPbI_3$-$DVL_{0.8}GCL_{0.2}$ under forward and reverse voltage bias (Figure S19f) exhibits excellent symmetry, in stark contrast to those grown in GBL and DVL. This suggests suppressed ion migration in $MAPbI_3$-$DVL_{0.8}GCL_{0.2}$ under an electric field.

The least defective crystalline structure of $MAPbI_3$-$DVL_{0.8}GCL_{0.2}$ leads to significantly enhanced stability compared to control samples. Figures 3g and S24 show a comparison of XRD spectra for three SC samples collected during ambient storage at room temperature and a high relative humidity over 150 days. No apparent phase transition was observed for $MAPbI_3$-$DVL_{0.8}GCL_{0.2}$ over this entire period, while the peaks of $MAPbI_3$-DVL and $MAPbI_3$-GBL disappeared after only 5 and 8 days, respectively. The high crystalline quality of $MAPbI_3$-$DVL_{0.8}GCL_{0.2}$ is also manifested in its optical properties and x-ray photoelectron spectroscopy, as discussed in Supporting Note 4 (Figures S25 and S26). In summary, the elevated mean steric hindrance of the solvent slows down the growth rate, thereby significantly increasing the crystalline quality.

2.4 | Performance of Photodetectors and X-Ray Detectors

The ability to grow high-quality MHP-SCs in a sterically optimized mixed solvent system at comparatively low temperatures and with a rapid growth rate provides a robust material foundation for developing high-performance optoelectronic devices. To showcase the potential of these as-grown MHP-SCs, we

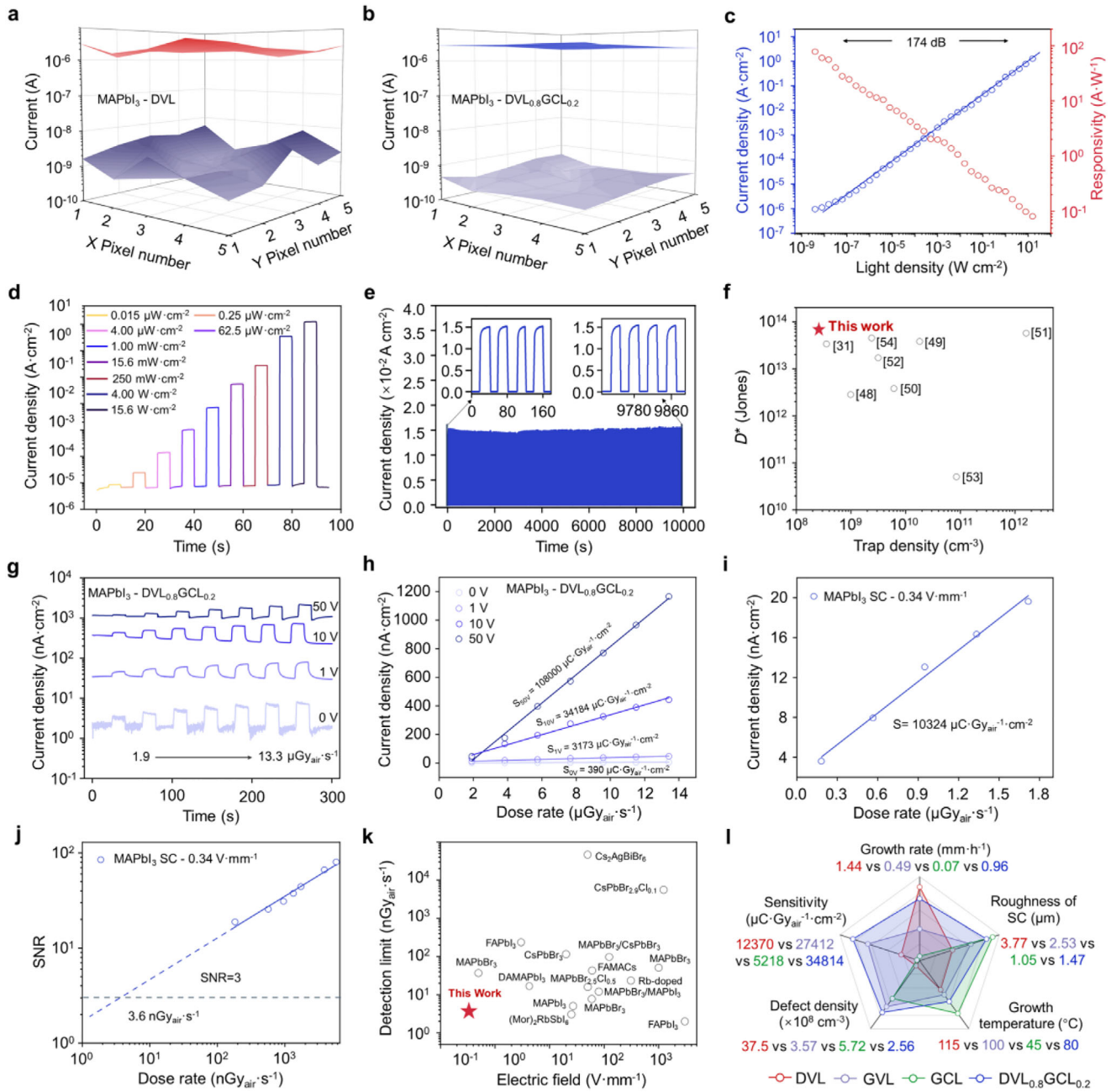

FIGURE 4 | Characterization of $MAPbI_3$-$DVL_{0.8}GCL_{0.2}$-SC photodetector and x-ray detector. (a) Performance comparison of photodetector arrays fabricated from $MAPbI_3$-DVL and (b) $MAPbI_3$- $DVL_{0.8}GCL_{0.2}$ under identical illumination conditions (650 nm, 50 mW cm^{-2}). (c) Current density and responsivity of photodetector against light power density. (d) Time-dependent current curves for $MAPbI_3$ SC photodetector under a series of light illumination intensities. (e) Current density of photodetector in continuous operation of 10 000 s. f Statistical comparison of trap densities and D^* of $MAPbI_3$-$DVL_{0.8}GCL_{0.2}$ and D^* of corresponding photodetectors from this work versus literature reports (data summarized in Table S11), highlighting the superior performance achieved with steric-hindrance-regulated crystal growth. (g) Voltage-dependent switching responses and (h) sensitivity of the x-ray detector as a function of x-ray dose rate from 1.9 μGy_{air} s^{-1} to 13.3 μGy_{air} s^{-1}. (i) Current density and (j) signal-to-noise ratio of the detector measured at various x-ray dose rates under low electric field conditions. (k) Comparison of detection limits reported in the literature with the $MAPbI_3$-$DVL_{0.8}GCL_{0.2}$-based x-ray detector developed in this work (data summarized in Table S12), demonstrating the state-of-the-art sensitivity achieved through steric-hindrance-guided crystal engineering. (l) Comparison of key parameters of $MAPbI_3$ SCs grown in DVL, GVL, GCL, and $DVL_{0.8}GCL_{0.2}$. For trap density and surface roughness, an inverted axis is used because lower values indicate higher crystal quality.

engineered photodetectors and x-ray sensors using the $MAPbI_3$-$DVL_{0.8}GCL_{0.2}$ SCs.

Figures 4a,b and S27 illustrate the structure of a photodetector featuring $MAPbI_3$-$DVL_{0.8}GCL_{0.2}$ (see detailed preparation and measurement of the device in characterizations and Supporting Note 5). Assessment of photodetector array uniformity using 5 × 5 pixel arrays configured from 6 × 6 electrodes, with each pixel defined by adjacent electrodes. Figure 4b illustrates the array's current variation under dark conditions and 650 nm illumination

(50 mW cm^{-2}), with each square representing a pixel. Detailed photocurrent/dark current fluctuations per pixel are shown in Figure S28. The $MAPbI_3$-$DVL_{0.8}GCL_{0.2}$ device exhibits minimal inter-pixel current fluctuation, in stark contrast to $MAPbI_3$-DVL. This is attributed to reduced crystal defect density, which enhances structural and charge distribution homogeneity—a direct indicator of superior electrical uniformity [45].

Because the $MAPbI_3$-$DVL_{0.8}GCL_{0.2}$ showed superior overall crystal quality compared with crystals grown in other solvent ratios, the corresponding device was chosen for further optoelectronic performance testing. The photodetector demonstrated broadband responsiveness from 365 nm to 808 nm (Figure S29). Photocurrent scales linearly with incident power density (0.06–1.92 mW cm^{-2}), peaking at 650 nm. Subsequent characterization therefore focused on 650 nm illumination. As shown in Figure S30, at a bias voltage of 3 V, the current density increased linearly from 2.4×10^{-6} to 1.26 A cm^{-2} as the optical power density increases from 3.1×10^{-8} to 15.6 W cm^{-2}, achieving a linear dynamic range (LDR) of 174 dB. The LDR could be further extended, as no deviation from linearity has yet been observed with increasing optical power density (Figure 4c). Furthermore, the detector exhibits fast response characteristics, with a rise time of 125 µs and a fall time of 273 µs (Figure S31a), suggesting efficient charge transport and suppressed ion migration. The −3 dB bandwidth was subsequently measured to evaluate the frequency response of the device, defined by the relative photoresponse as a function of frequency (Figure S31b). Under 650 nm laser illumination with a power density of 50 mW cm^{-2}, the $MAPbI_3$-$DVL_{0.8}GCL_{0.2}$ detector showed a −3 dB cutoff frequency of 2000 Hz. To further evaluate its detection capability, noise current density measurements were performed, as shown in Figure S32. The $MAPbI_3$-$DVL_{0.8}GCL_{0.2}$ device exhibited a low noise current spectral density of 8.9×10^{-15} A $Hz^{-0.5}$ at a frequency of 300 Hz. The responsivity, external quantum efficiency (EQE), and specific detectivity (D^*) are presented in Figures 4c and S33. At a low optical power density of 3.9×10^{-9} W cm^{-2}, the photodetector exhibits a responsivity of 78.3 A W^{-1}, an EQE of 14 929%, and a D^* of 6.81×10^{13} Jones. Figure 4d demonstrates the switching response of the photodetector at power densities ranging from 1.5×10^{-8} to 15.6 W cm^{-2}. At the highest power density of 15.6 W cm^{-2}, the photodetector achieves a switching ratio of 1.4×10^6. The exceptionally high switching ratio at elevated optical power density is mainly attributed to the suppressed dark current and enhanced photocurrent arising from the low defect density of $MAPbI_3$-$DVL_{0.8}GCL_{0.2}$.

The photodetector demonstrates exceptional operational stability (Figure 4e). Under continuous 3.15×10^{-3} W cm^{-2} illumination and 3 V bias, the photocurrent density remains stable over 10^4 s (≈500 cycles). After 2-month ambient storage, the dark current at 2 V increased marginally from 1.12×10^{-10} to 1.23×10^{-10} A, while the photocurrent decreased slightly from 5.15×10^{-8} A to 5.08×10^{-8} A. The switching ratio exhibited only 9% degradation, demonstrating robust environmental stability (Figure S34). Figure 4f compares the trap density of $MAPbI_3$-$DVL_{0.8}GCL_{0.2}$ and the D^* of its corresponding photodetector with those of other $MAPbI_3$ SCs and their devices reported in the literature (Table S11) [29, 46–52]. $MAPbI_3$-$DVL_{0.8}GCL_{0.2}$ shows the lowest trap density alongside a relatively high D^*. Although no simple linear dependence between trap density and D^* is observed, a low trap density favors high D^* by reducing trap-assisted carrier recombination and carrier loss, as well as dark current and noise. Nevertheless, D^* is also governed by device architecture, carrier collection efficiency, and noise characteristics, and therefore cannot be directly predicted from trap density alone. The comparison in Figure 4f, thus, highlights the contribution of crystal quality to device performance rather than demonstrating a definite relationship between trap density and D^*. Notably, the crystal thickness used in this work exceeds the ideal value for photodetectors, suggesting that further optimization of the device thickness and architecture could potentially improve the device performance.

Figure S35 shows the structure of a $MAPbI_3$-$DVL_{0.8}GCL_{0.2}$-based x-ray detector, which adopts a multilayer Au/SC/C_{60}/Cr configuration. Figure 4g shows the current density switching curves of the device under x-ray doses ranging from 1.9 µGy_{air} s^{-1} to 13.3 µGy_{air} s^{-1} at different reverse bias voltages. The sensitivity of the detector was calculated using $S = Q/(A \cdot X)$, where S is the detector sensitivity, Q is the collected charge during irradiation, X is the received radiation dose rate, and A is the irradiated area. The sensitivities at bias voltages of 0, 1, 10, and 50 V were 390, 3173, 34 184, and 108 000 µC Gy_{air}^{-1} cm^{-2}, respectively (Figure 4h). These values surpass those based on $MAPbI_3$ SCs grown in pure solvents: at 10 V, the sensitivities of $MAPbI_3$-DVL, $MAPbI_3$-GVL, and $MAPbI_3$-GCL detectors were 12 370, 27 412, and 5138 µC Gy_{air}^{-1} cm^{-2} corresponding to 36%, 80%, and 15% of the $MAPbI_3$-$DVL_{0.8}GCL_{0.2}$ detector, respectively. The complete switching responses and sensitivity curves are provided in Figure S36. This direct comparison indicates that the optimized mixed-solvent system outperforms the benchmark GVL system at the device level.

The $MAPbI_3$-$DVL_{0.8}GCL_{0.2}$ x-ray detector demonstrates a linear response under low electric fields, with current density increasing proportionally from 3.60 µA cm^{-2} to 19.62 µA cm^{-2} as the x-ray dose rate rises from 0.18 µGy_{air} s^{-1} to 1.72 µGy_{air} s^{-1}. Linear fitting reveals a high sensitivity of 1.03×10^4 µC Gy_{air}^{-1} cm^{-2} even at a low electric field strength of 0.34 V mm^{-1} (Figure 4i). The device response under varying field strengths and dose rates is shown in Figure S37. The limit of detection (LoD) of the as-prepared detector is as low as 3.6 nGy_{air} s^{-1} (Figure 4j), equivalent to just 1/1596 of the standard medical diagnostic dose rate. For x-ray detection, the capability to sense weak signals with high sensitivity is critical. As shown in Figure 4k, comparison of LoD and operating field strengths among reported MHP-SC-based x-ray detectors (Table S11) places the $MAPbI_3$-$DVL_{0.8}GCL_{0.2}$ detector among the devices with the lowest reported LoD under low electric fields [16, 47, 53–66]. To further evaluate the low-dose rate imaging capability, x-ray imaging was performed at a dose rate of 420 nGy_{air} s^{-1}, within the sub-µGy_{air} s^{-1} regime. The obtained image shows that the detector can produce usable imaging contrast under low radiation flux (Figure S38). We note that this imaging dose rate is higher than the electrical LoD because image formation requires spatially resolved contrast and sufficient signal integration. Finally, we systematically compared the performance of SCs grown from DVL, GVL, GCL, and the $DVL_{0.8}GCL_{0.2}$ mixed-solvent system (Figure 4l), including key performance metrics of the x-ray detectors. The results show that the $DVL_{0.8}GCL_{0.2}$ offers superior overall properties in terms of defect suppression, and signal response while maintaining a

balanced crystal growth rate, further highlighting the advantages of the mixed-solvent strategy.

2.5 | Flexibility and Universality of Steric Hindrance Engineering

We demonstrate that steric hindrance engineering greatly enhances both the flexibility and universality of the ITC method. By tuning the DVL-GCL ratios (ranging from pure DVL to $DVL_{0.5}GCL_{0.5}$), we established a green solvent system with adjustable steric environments and systematically grew a wide range of MHP-SCs with diverse A-site cations and halides. These include mixed-halide ($MAPbX_3$, X = Cl, Br, I) as detailed in Supporting Note 6 and Figure S39, mixed-A-site and B-site ($MAPb_xZn_{1-x}I_3$, $FA_xMA_{1-x}PbI_3$, $[MAPbI_3]_x[MA_3Bi_2I_9]_{1-x}$, $[MAPbI_3]_x[PEA_2PbI_4]_{1-x}$, and $[MAPbI_3]_x[FPEA_2PbI_4]_{1-x}$), and Pb-free MHP-SCs ($MASnI_3$ and $FASnI_3$). The detailed growth parameters for these MHP-SCs are summarized in Table S13. In all cases, high-quality crystals with consistent growth rates of ~0.5 mm h^{-1} were achieved using sterically optimized mixed solvents, underscoring the broad effectiveness and generality of steric hindrance engineering in ITC-based MHP-SC synthesis.

3 | Conclusion

In this work, within the framework of green chemistry, we present an environmentally sustainable and efficient strategy for the growth of MHP-SCs by integrating green solvent selection with a novel crystallization-control approach based on steric hindrance engineering. Conventional high-toxicity solvents were replaced by bio-derived, low-toxicity lactone solvents, DVL and GCL, both exhibiting high GSK green solvent scores (>7). These solvents feature closely matched DN and boiling points, yet distinct molecular spatial configurations. This work unveils the critical role of steric effects of solvent molecules, rather than conventional Lewis basicity, in governing crystallization dynamics. By adjusting their volume ratio of DVL and GCL, we precisely tuned the mean steric hindrance of the solvent system without significantly altering its mean Lewis basicity, thereby regulating the Pb^{2+}-solvent coordination strength and crystallization kinetics, which is similar to adjusting the DN values while avoiding volatility imbalance.

Implementing this steric hindrance engineering within the ITC process enables highly reproducible and rapid crystal growth. The resulting $MAPbI_3$ SCs exhibit exceptional structural quality, evidenced by a narrow XRD rocking curve linewidth of 0.00802° and an ultralow trap density of 2.56×10^8 cm^{-3}. These superior structural properties translate into outstanding optoelectronic performance: photodetectors based on these crystals achieve a detectivity of 6.81×10^{13} Jones at 650 nm, and x-ray detectors demonstrate a low detection limit of 3.6 nGy_{air} s^{-1}, which is significantly below the standard medical diagnostic threshold. Moreover, the devices show robust operational and environmental stability.

Beyond achieving high performance, the universality of this steric hindrance engineering strategy is demonstrated across diverse perovskite compositions, including inorganic, low-dimensional, and lead-free perovskites. These findings establish a scalable and sustainable blueprint for producing high-quality MHP-SCs, highlighting how green chemistry principles can synergize with advanced materials engineering to drive the development of next-generation optoelectronic devices.

4 | Materials and Methods

4.1 | Material

Methylammonium iodide (MAI, 99.5%), methylammonium bromide (MABr, 99.5%), cesium iodide (CsI, > 99.99%), and phenylethylammonium iodide (PEAI, 99.5%) were procured from Xi'an Yuri Solar Co., Ltd.; lead (II) bromide ($PbBr_2$, 99.0%); tin (II) iodide (SnI_2, 99.99%) were obtained from Aladdin; lead (II) iodide (PbI_2, 99%+) and cyclohexanone (99%+) were sourced from Adamas-beta; fluorophenylethylammonium iodide (F-PEAI, 99%) was purchased from APINNO; zinc iodide (ZnI_2, 99.9%) was obtained from Aladdin; formamidinium iodide (FAI, 99.5%) was purchased from Shanghai Macklin Biochemical Technology Co., Ltd.; γ-butyrolactone (GBL, 99%), ethyl acetate (≥99.5%), methyl acetate (≥99.5%), and acetone (≥99.5%) were procured from Sinopharm Chemical Reagent Co., Ltd.; γ-valerolactone (GVL, ≥99%) and *N*,*N*-dimethylformamide (DMF, ≥99%) were sourced from Solarbio; δ-valerolactone (DVL, 98%) was obtained from Energy Chemical; γ-caprolactone (GCL, 98%) was purchased from ACMEC Biochemical; cyclopentanol (99%) and cyclopentanone (99.5%) were purchased from ACMEC Biochemical. All raw materials and solvents were used as received without further purification.

4.2 | Growth of MHP-SC in Steric-Engineered Solvent via ITC

Figure S1 depicts the schematic growth process of $MAPbI_3$ SCs in a steric hindrance-optimized DVL-GCL mixed solvent. The growth initiated With the dissolution of MAI and PbI_2 in a $DVL_{0.8}GCL_{0.2}$ solution maintaining a molar ratio of 1.1:1, with excess MAI ensuring complete PbI_2 transformation into $MAPbI_3$. After 1 h of vigorous stirring, a clear solution was obtained. Seed crystals were prepared by heating 0.5 mL of this precursor solution at 45°C–110°C for 20 min. Subsequently, 2 mL of the solution was filtered Through a 0.22 μm nylon filter and used for ITC. A meticulously selected small yet fully formed seed crystal was introduced Into the filtered solution and heated at 45°C–110°C for several hours. Post-growth, the $MAPbI_3$ SCs were cleaned with acetone and vacuum-dried for 2 h. Table S13 summarizes the precursor concentrations, T_G, growth rates in various pure and mixed solvents, and the root-mean-square roughness R_q of the resultant $MAPbI_3$ SCs.

4.3 | Theoretical Calculations

4.3.1 | Software Employed in the Calculations

DFT calculations were performed using Gaussian 16 software [67], the AIMD simulations were conducted with CP2K software [68], and ESP and molecular volume were analyzed using

Multiwfn 3.8 (dev) [69, 70]. All molecular structures were visualized using VMD software [71].

4.4 | Characterizations

4.4.1 | Steady-State and Time-Resolved Photoluminescence

Steady-state photoluminescence spectra and time-resolved photoluminescence spectra were obtained using an FLS-1000 fluorescence spectrometer, excited at a wavelength of 405 nm.

4.4.2 | Fourier Transform Infrared Spectroscopy

Fourier transform infrared spectroscopy (Microet IS10) was utilized to elucidate the infrared spectrum of the precursor solution. Field emission scanning electron microscopy (SURA55 Sapphire) was employed to characterize the initial crystal size and elemental composition of the $MAPbX_3$ crystals.

4.4.3 | X-Ray Photoelectron Spectroscopy

X-ray photoelectron spectroscopy was performed using an Escalab Xi+ (Thermo Fisher) instrument equipped with an Al Kα x-ray source (1486.68 eV) to analyze the elemental composition and chemical states of the $MAPbX_3$ SCs.

4.4.4 | Surface Morphology

The surface morphology of the MHP-SCs was analyzed using a laser confocal microscope (LSM900), from which the overall roughness was calculated. Additionally, the local roughness at the nanoscale was further characterized with a high-resolution, environment-controlled atomic force microscope (Cypher ES).

4.4.5 | MHP-SCs Growth Rate Test

Uniform seed crystals were selected and immersed in precursor solutions with varying solvent compositions for ITC growth. Crystal dimensions were periodically recorded through imaging, and growth rates were determined by linear fitting of crystal length versus time data.

4.4.6 | Solubility Test

Solubility testing was performed on $MAPbI_3$ powder derived from ground as-grown $MAPbI_3$ SCs. Various solvents were placed in small bottles and heated to specific temperatures, such as 80°C. $MAPbI_3$ powder was gradually added while stirring, and saturation was deemed to be reached when the solvent could no longer dissolve additional powder. The hot solution was filtered for clarity, followed by complete evaporation of the solvent under heat, and the remaining $MAPbI_3$ mass was measured to calculate solubility at the specific temperature. This process was repeated for DVL, $DVL_{0.8}GCL_{0.2}$, and GCL at different temperatures. The upper limit of the metastable region was estimated by observing the spontaneous crystallization temperature of solutions with varying concentrations. This upper limit provides a schematic representation of the supersolubility curve.

4.4.7 | X-Ray Diffraction

X-ray diffraction patterns of $MAPbI_3$ SCs and powders were collected using a Shimadzu x-ray diffractometer (Shimadzu, Japan) equipped with Cu Kα radiation (operating at 40 kV and 40 mA). The powder samples were thoroughly ground and sieved through a 200-mesh screen to ensure uniform particle size prior to analysis. The rocking curves of the $MAPbI_3$ SCs were characterized using a Rigaku SmartLab diffractometer (3 kW, Japan) with a tube voltage of 30 kV and a current of 20 mA.

4.4.8 | UV–Vis-NIR Absorbance Spectra

The absorption spectra of $MAPbI_3$ SC powders and the $MAPbI_3$ precursor were measured using a PerkinElmer LAMBDA 1050+ UV–vis-NIR spectrophotometer. The spectral range extended from 300 nm to 850 nm, and measurements were carried out at room temperature. Before testing, all $MAPbI_3$ precursor solutions were diluted to a uniform concentration of 0.05 mmol L^{-1}.

4.4.9 | Scanning Electron Microscope and Energy Dispersive X-Ray Spectroscopy

Energy dispersive x-ray spectroscopy was conducted using the integrated module of a field emission scanning electron microscope (FESEM, SUPRA 55 Sapphire) for quantitative analysis of the elemental composition of MHP-SCs. The analysis was performed at an acceleration voltage of 20 kV with a working distance of 8.5 mm.

4.4.10 | Transmission Electron Microscope

Transmission electron microscope (TEM, JEOL JEM-2100plus) was used to examine the initial crystal sizes of $MAPbI_3$ and $MAPbBr_3$ SCs.

4.4.11 | Nuclear Magnetic Resonance

A fully digital nuclear magnetic resonance spectrometer (Bruker Avance neo 500) was used to measure the chemical shifts of Pb in various precursors. Saturated precursor solutions were used to enhance the signal strength.

4.4.12 | Determination of DN

The DN of the solvent was determined through linear fitting of the ^{23}Na NMR spectra of a 10 mM NaTFSI/solvent solution, following the method introduced by Johnson et al. [72].

4.4.13 | Deep-Level Transient Spectroscopy

Deep-level transient spectroscopy measurements were performed using a deep-level transient spectroscopy system (FT1030, Phystech, Germany). A high-frequency signal of 100 mV at 1 MHz was applied. The capacitance measurement range was 0–8000 pF, with an automatic reverse-bias capacitance compensation range of 0–6000 pF and automatic range switching. The capacitance resolution was 0.01 fF. The measurement conditions were as follows: the time window was 50.18 ms, the filling pulse width was 10 ms, the reverse bias was −2 V, and the pulse voltage was 0.5 V. The temperature range was 80–350 K.

4.4.14 | Thermal Admittance Spectroscopy

The C–f measurements were performed by a precision LCR Meter (6500b Series). The AC frequency range for the capacitance was from 30 Hz to 100 MHz.

4.4.15 | Measurement of the Mobility-Lifetime Product of $MAPbI_3$ SC Detectors

The $\mu\tau$ product was extracted from laser-induced photocurrent transport measurements. A continuous-wave semiconductor laser with a wavelength of 650 nm was used as the excitation source to generate electron-hole pairs in $MAPbI_3$ SCs. The laser was incident perpendicularly onto the active area with a spot size of ~10 mm^2 and a power density of 100 mW cm^{-2} to ensure operation in the linear response regime while minimizing thermal effects. Steady-state photocurrent responses were recorded under bias voltages from 0 V to 100 V. The $\mu\tau$ product was determined by fitting the carrier collection behavior using the Hecht equation.

4.5 | Fabrication and Performance Measurement of Photodetectors

Using a 200-mesh copper grid as a stencil, a 50-nm-thick gold electrode array was deposited onto the crystal surface via thermal evaporation using the FS450-S8 thin film deposition system. The spacing between adjacent gold electrodes was 15 μm, resulting in an effective light-receiving area of 3.22×10^{-5} cm^2. For low power density (0.0001–500 μW cm^{-2}) photoresponse measurements, a 650 nm LED light source (SangNon SN-M11) was used. In contrast, for high power density (0.5 to 1.6×10^4 mW cm^{-2}) photoresponse tests, a 650-nm laser (Xi'an Leixin Yangxiang Optoelectronic Technology Co., Ltd., 650 nm, 100 mW) was employed. The optical power of the 650 nm light was quantified using a Thorlabs PM100D optical powermeter. The optical response of the device under varying optical power densities was evaluated using a semiconductor parameter analyzer and a semiconductor device measurement station, with a voltage sampling interval of 0.05 V to ensure data accuracy. Noise current was measured at different frequency using a spectrum analyzer (Agilent 35670A) with a low-noise current preamplifier (Stanford Research System, SR570). The transient photoresponse was recorded using a 650 nm nanosecond light source integrated into an FLS1000 spectrometer and monitored with an Agilent DSOX2002A digital oscilloscope.

4.6 | Fabrication and Performance Measurement of X-Ray Detectors

The x-ray detectors feature multilayered structure of Au/SC/C_{60}/Cr. Au, C_{60}, and Cr films with thickness of 50, 20, and 80 nm were prepared by thermal evaporation using the FS450-S8 thin film deposition system. Photoconductive devices typically exhibit a significant dark current. To mitigate this, we incorporated a C_{60} thin layer between the perovskite and Cr electrode, serving as a barrier to external electron injection in dark conditions. The MGI 320 instrument, manufactured by YXLON, incorporates an x-ray tube with a tungsten target. The x-ray focal size, defined as the diameter of the metal target, is adjustable within a range of 0.4–1 mm. In this study, all x-ray experiments were conducted with a focal size setting of 1 mm. At this focal size, the diameter of the test area at a distance of 500 mm from the focal spot was measured to be 360 mm. The dose rate of the continuous x-ray beam can be incrementally adjusted by altering the tube voltage and tube current. For consistency, the tube voltage of the x-ray source was maintained at 120 kV, corresponding to a continuous x-ray spectrum with a maximum photon energy of 120 keV, while the dose rate was modulated by varying the tube current from 0.2 mA to 15 mA. Prior to x-ray characterization, the dose rate of the x-ray source was meticulously calibrated at each tube current setting using the IBA MagicMaX Multi-Detector (XR 40–150 kV). Additionally, a Keithley 2400 sourcemeter was employed to apply a bias voltage ranging from 0 V to 200 V. The low-noise current preamplifier (SR570, Stanford Research Systems) and SR830 lock-in amplifier were subsequently utilized to accurately record the signals.

Supporting Information

Details of theoretical calculations; details of inverse temperature crystallization; description on the limit of Lewis theory; characteristics of $MAPbI_3$ SCs; characterizations of photodetector and x-ray detector; solvent steric hindrance engineering modulating growth of MHP-SCs; other data.

Author Contributions

Y.L. and S.W. conceived and supervised the project. T.Z. synthesized the MHP-SCs and performed the measurements. Y.H. carried out the theoretical calculations. J.H. investigated and discussed the crystal growth mechanism, analyzed and interpreted the FTIR spectra, and conducted the x-ray detection experiments with H.W. D.C. and Y.L. conducted the noise current measurements and thermal admittance spectroscopy. X.C. synthesized the MHP-SCs. G.C. provided technical support. X.F., Q.Z., T.-W.L., and Z.C. analyzed the data. R.Z. assisted with experimental measurements and data analysis. X.Y. and Y.Z. performed optical measurements. Y.L. and S.W. co-wrote the manuscript, which was revised by T.-W.L. All authors discussed the results and contributed to the manuscript.

Acknowledgements

This work is supported by the National Natural Science Foundation of China (62374142, 52303380, and 52573274), the Fundamental and Interdisciplinary Disciplines Breakthrough Plan of the Ministry of Education of China (JYB2025XDXM401), the Fundamental Research Funds for the Central Universities (20720240064, 20720240041, and 20720250124),

the External Cooperation Program of Fujian (2022I0004), the Major Science and Technology Project of Xiamen in China (3502Z20191015), the Fujian Provincial Natural Science Foundation of China (2025J08019), the Natural Science Foundation of Xiamen, China (3502Z202471002), and the 2024 Key Technological Innovation and Industrialization Project of Fujian Province (No.2024G021). Q.Z. acknowledges support from Research Institute of Adv. Mater. (RIAM). We thank Mr. Wei Yan for his assistance on photographing the samples.

Conflicts of Interest

The authors declare no conflicts of interest.

Data Availability Statement

All data supporting the findings of this study are available in the manuscript and its Supporting Information. Other related raw data are fully and freely available from the corresponding authors.

References

1. Y. Lei, Y. Chen, R. Zhang, et al., "A Fabrication Process for Flexible Single-Crystal Perovskite Devices," *Nature* 583 (2020): 790–795, https://doi.org/10.1038/s41586-020-2526-z.

2. W. Chen, Z. Huang, H. Yao, et al., "Highly Bright and Stable Single-Crystal Perovskite Light-Emitting Diodes," *Nature Photonics* 17 (2023): 401–407, https://doi.org/10.1038/s41566-023-01167-3.

3. H. Cho, S.-H. Jeong, M.-H. Park, et al., "Overcoming the Electroluminescence Efficiency Limitations of Perovskite Light-Emitting Diodes," *Science* 350 (2015): 1222–1225, https://doi.org/10.1126/science.aad1818.

4. J. S. Kim, J.-M. Heo, G.-S. Park, et al., "Ultra-Bright, Efficient and Stable Perovskite Light-Emitting Diodes," *Nature* 611 (2022): 688–694, https://doi.org/10.1038/s41586-022-05304-w.

5. Y. Xiong, X. Xu, B. Chen, and X. Xu, "Highly Crystalized $MAPbX_3$ Perovskite Triangular Nanowire Arrays for Optoelectronic Applications," *Advanced Materials* 36 (2024): 2310427, https://doi.org/10.1002/adma.202310427.

6. W. Deng, J. Jie, X. Xu, et al., "A Microchannel-Confined Crystallization Strategy Enables Blade Coating of Perovskite Single Crystal Arrays for Device Integration," *Advanced Materials* 32 (2020): 1908340, https://doi.org/10.1002/adma.201908340.

7. J. Jiang, M. Xiong, K. Fan, et al., "Synergistic Strain Engineering of Perovskite Single Crystals for Highly Stable and Sensitive X-Ray Detectors With Low-Bias Imaging and Monitoring," *Nature Photonics* 16 (2022): 575–581, https://doi.org/10.1038/s41566-022-01024-9.

8. K. Sakhatskyi, B. Turedi, G. J. Matt, et al., "Stable Perovskite Single-Crystal X-Ray Imaging Detectors With Single-Photon Sensitivity," *Nature Photonics* 17 (2023): 510–517, https://doi.org/10.1038/s41566-023-01207-y.

9. Y. Liu, Z. Yang, D. Cui, et al., "Two-Inch-Sized Perovskite $CH_3NH_3PbX_3$ (X = Cl, Br, I) Crystals: Growth and Characterization," *Advanced Materials* 27 (2015): 5176–5183, https://doi.org/10.1002/adma.201502597.

10. L. Ma, Z. Yan, X. Zhou, et al., "A Polymer Controlled Nucleation Route Towards the Generalized Growth of Organic–Inorganic Perovskite Single Crystals," *Nature Communications* 12 (2021): 2023, https://doi.org/10.1038/s41467-021-22193-1.

11. L. Zhao, Z. Shi, Y. Zhou, et al., "Surface-Defect-Passivation-Enabled Near-Unity Charge Collection Efficiency in Bromide-Based Perovskite Gamma-Ray Spectrum Devices," *Nature Photonics* 18 (2024): 250–257, https://doi.org/10.1038/s41566-023-01356-0.

12. S. Sánchez, L. Pfeifer, N. Vlachopoulos, and A. Hagfeldt, "Rapid Hybrid Perovskite Film Crystallization From Solution," *Chemical Society Reviews* 50 (2021): 7108–7131, https://doi.org/10.1039/D0CS01272F.

13. J. Li, Z. Han, Y. Gu, et al., "Perovskite Single Crystals: Synthesis, Optoelectronic Properties, and Application," *Advanced Functional Materials* 31 (2021): 2008684, https://doi.org/10.1002/adfm.202008684.

14. J. Sun, R. Li, Y. Gui, X. Shao, J. Xue, and R. Wang, "Mechanistic Insights and Optimization Strategies for Perovskite Single-Crystal Thin Film Growth," *Chemical Science* 16 (2025): 6188–6202, https://doi.org/10.1039/D4SC08145E.

15. Y. Miao, M. Ren, Y. Chen, et al., "Green Solvent Enabled Scalable Processing of Perovskite Solar Cells With High Efficiency," *Nature Sustainability* 6 (2023): 1465–1473, https://doi.org/10.1038/s41893-023-01196-4.

16. D. Chu, N. Liu, S. Xie, et al., "Stable and Ultrasensitive X-Ray Detectors Based on Oriented Single-Crystal Perovskite Rods," *Advanced Materials* 37 (2025): 2500101, https://doi.org/10.1002/adma.202500101.

17. L. Zhao, Y. Zhou, Z. Shi, et al., "High-Yield Growth of $FACsPbBr_3$ Single Crystals With Low Defect Density From Mixed Solvents for Gamma-Ray Spectroscopy," *Nature Photonics* 17 (2023): 315–323.

18. J. S. Manser, M. I. Saidaminov, J. A. Christians, O. M. Bakr, and P. V. Kamat, "Making and Breaking of Lead Halide Perovskites," *Accounts of Chemical Research* 49 (2016): 330–338, https://doi.org/10.1021/acs.accounts.5b00455.

19. A. Curzons, D. Constable, and V. Cunningham, "Solvent Selection Guide: a Guide to the Integration of Environmental, Health and Safety Criteria Into the Selection of Solvents," *Clean Technologies and Environmental Policy* 1 (1999): 82–90, https://doi.org/10.1007/s100980050014.

20. C. M. Alder, J. D. Hayler, R. K. Henderson, et al., "Updating and Further Expanding GSK's Solvent Sustainability Guide," *Green Chemistry* 18 (2016): 3879–3890, https://doi.org/10.1039/C6GC00611F.

21. R. G. Dastidar, J. E. Chavarrio, Z. Jiang, D. J. McClelland, M. Mavrikakis, and G. W. Huber, "Catalytic Production of δ-Valerolactone (DVL) From Biobased 2-Hydroxytetrahydropyran (HTHP)—Combined Experimental and Modeling Study," *Applied Catalysis B: Environment and Energy* 360 (2025): 124519, https://doi.org/10.1016/j.apcatb.2024.124519.

22. S. Gupta, R. Arora, N. Sinha, M. I. Alam, and M. A. Haider, "Mechanistic Insights Into the Ring-Opening of Biomass Derived Lactones," *RSC Advances* 6 (2016): 12932–12942, https://doi.org/10.1039/C5RA22832H.

23. D. J. Kubicki, S. D. Stranks, C. P. Grey, and L. Emsley, "NMR Spectroscopy Probes Microstructure, Dynamics and Doping of Metal Halide Perovskites," *Nature Reviews Chemistry* 5 (2021): 624–645, https://doi.org/10.1038/s41570-021-00309-x.

24. J. Cao, W. Zhan, M. Ren, et al., "High-Brightness Perovskite Light-Emitting Diodes With Suppressed Efficiency Roll-Off Using the Green Solvent γ-Valerolactone," *ACS Nano* 19 (2025): 9053–9060, https://doi.org/10.1021/acsnano.4c17765.

25. J. Kim, B.-W. Park, J. Baek, et al., "Unveiling the Relationship Between the Perovskite Precursor Solution and the Resulting Device Performance," *Journal of the American Chemical Society* 142 (2020): 6251–6260, https://doi.org/10.1021/jacs.0c00411.

26. W. Wang, H. Meng, H. Qi, et al., "Electronic-Grade High-Quality Perovskite Single Crystals by a Steady Self-Supply Solution Growth for High-Performance X-Ray Detectors," *Advanced Materials* 32 (2020): 2001540, https://doi.org/10.1002/adma.202001540.

27. N. Li, A. Feng, X. Guo, et al., "Engineering the Hole Extraction Interface Enables Single-Crystal $MAPbI_3$ Perovskite Solar Cells With Efficiency Exceeding 22% and Superior Indoor Response," *Advanced Energy Materials* 12 (2022): 2103241, https://doi.org/10.1002/aenm.202103241.

28. Y. Liu, Y. Zhang, X. Zhu, et al., "Inch-Sized High-Quality Perovskite Single Crystals by Suppressing Phase Segregation for Light-Powered Integrated Circuits," *Science Advances* 7 (2021): abc8844.

29. Z. Li, S. Sun, H. Jiang, et al., "γ-Valerolactone Enabling Spontaneously Inhibited Iodide Oxidation for High-Quality Perovskite Single Crystal Fabrication," *Advanced Functional Materials* 34 (2024): 2407629, https://doi.org/10.1002/adfm.202407629.

30. Y. Zhang, Y. Liu, Z. Xu, et al., "Nucleation-Controlled Growth of Superior Lead-Free Perovskite $Cs_3Bi_2I_9$ Single-Crystals for High-Performance

X-Ray Detection," *Nature Communications* 11 (2020): 2304, https://doi.org/10.1038/s41467-020-16034-w.

31. L. Liu, S.-Y. Liu, Y. Shi, et al., "Anti-Perovskites With Long Carrier Lifetime for Ultralow Dose and Stable X-Ray Detection," *Nature Photonics* 18 (2024): 990–997, https://doi.org/10.1038/s41566-024-01482-3.

32. Y. Liang, F. Li, X. Cui, et al., "Toward Stabilization of Formamidinium Lead Iodide Perovskites by Defect Control and Composition Engineering," *Nature Communications* 15 (2024): 1707, https://doi.org/10.1038/s41467-024-46044-x.

33. Y. Hua, G. Zhang, X. Sun, et al., "Suppressed Ion Migration for High-Performance X-Ray Detectors Based on Atmosphere-Controlled EFG-Grown Perovskite $CsPbBr_3$ Single Crystals," *Nature Photonics* 18 (2024): 870–877, https://doi.org/10.1038/s41566-024-01480-5.

34. Z. Wang, C. Shan, C. Liu, et al., "In Situ Growth of Perovskite Single-Crystal Thin Films With Low Trap Density," *Cell Reports Physical Science* 4 (2023): 101363.

35. D. Liu, Y. Zheng, X. Y. Sui, et al., "Universal Growth of Perovskite Thin Monocrystals From High Solute Flux for Sensitive Self-Driven X-Ray Detection," *Nature Communications* 15 (2024): 2390, https://doi.org/10.1038/s41467-024-46712-y.

36. Y. Liu, T. Ma, C. Wang, et al., "Synergistic Immobilization of Ions in Mixed Tin-Lead and All-Perovskite Tandem Solar Cells," *Nature Communications* 16 (2025): 3477, https://doi.org/10.1038/s41467-025-58810-6.

37. T. Yang, L. Gao, J. Lu, et al., "One-Stone-for-Two-Birds Strategy to Attain Beyond 25% Perovskite Solar Cells," *Nature Communications* 14 (2023): 839, https://doi.org/10.1038/s41467-023-36229-1.

38. S. Fu, S. Zhou, W. Meng, et al., "Piracetam Shapes Wide-Bandgap Perovskite Crystals for Scalable Perovskite Tandems," *Nature Nanotechnology* 20 (2025): 764–771, https://doi.org/10.1038/s41565-025-01899-z.

39. M. Li, Y. Jiang, S. Chen, et al., "Radical Molecular Network-Buffer Minimizes Photovoltage Loss in $FAPbI_3$ Perovskite Solar Cells," *Advanced Materials* 37 (2025): 2417289, https://doi.org/10.1002/adma.202417289.

40. L. L. Kerr, S. S. Li, S. W. Johnston, et al., "Investigation of Defect Properties in Cu (In, Ga) Se_2 Solar Cells by Deep-Level Transient Spectroscopy," *Solid-State Electronics* 48 (2004): 1579–1586, https://doi.org/10.1016/j.sse.2004.03.005.

41. A. Balcioglu, R. Ahrenkiel, and F. Hasoon, "Deep-Level Impurities in CdTe/CdS Thin-film Solar Cells," *Journal of Applied Physics* 88 (2000): 7175–7178, https://doi.org/10.1063/1.1326465.

42. C. Wang, S. Chen, J. Jie, et al., "Metal Halide Perovskite Single Crystals Toward Electroluminescent Applications," *Advanced Functional Materials* 35 (2025): 2401189, https://doi.org/10.1002/adfm.202401189.

43. W. Lian, C. Jiang, Y. Yin, et al., "Revealing Composition and Structure Dependent Deep-Level Defect in Antimony Trisulfide Photovoltaics," *Nature Communications* 12 (2021): 3260, https://doi.org/10.1038/s41467-021-23592-0.

44. G. Lindström, "Radiation Damage in Silicon Detectors," *Nuclear Instruments and Methods in Physics Research Section A: Accelerators, Spectrometers, Detectors and Associated Equipment* 512 (2003): 30–43, https://doi.org/10.1016/S0168-9002(03)01874-6.

45. X. Yang, Y. Song, L. Wang, et al., "In-line Tempering Eliminates the Domain Boundary in Perovskite Single Crystals for High–Energy Resolution Ionizing Radiation Detectors," *Science Advances* 10 (2024): eadq6866, https://doi.org/10.1126/sciadv.adq6866.

46. A. Gao, Y. Chen, Z. Li, et al., "Self-Cleaning Perovskite Single Crystals Fabricated With Bis(trifluoromethylsulfonyl)imide Derived Ionic Liquid Toward High-Performance Photodetection," *Advanced Functional Materials* 34 (2024): 2314237, https://doi.org/10.1002/adfm.202314237.

47. Y. Huang, L. Qiao, Y. Jiang, et al., "A-Site Cation Engineering for Highly Efficient $MAPbI_3$ Single-Crystal X-Ray Detector," *Angewandte Chemie International Edition* 58 (2019): 17834–17842, https://doi.org/10.1002/anie.201911281.

48. L. Zi, W. Xu, R. Sun, et al., "Lanthanide-Doped $MAPbI_3$ Single Crystals: Fabrication, Optical and Electrical Properties, and Multi-Mode Photodetection," *Chemistry of Materials* 34 (2022): 7412–7423, https://doi.org/10.1021/acs.chemmater.2c01549.

49. Y. Xiong, B. Chen, X. Xu, S. Dai, Y. Zhan, and X. Xu, "Facile Fabrication of Highly Crystallized, Air-Stable, and Flexible Perovskite Micromesh Film Photodetector," *Advanced Optical Materials* 12 (2024): 2401287, https://doi.org/10.1002/adom.202401287.

50. L. Liu, M. Xu, P. Cheng, et al., "Isotope Synergetic Effect on Hybrid Organic–Inorganic Perovskite Single Crystal Carrier Transport and High-Performance Photodetectors," *ACS Materials Letters* 6 (2024): 3834–3843, https://doi.org/10.1021/acsmaterialslett.4c00956.

51. Y. Sun, X. Liu, W. Deng, et al., "A Three-Dimensional Confined Crystallization Strategy Toward Controllable Growth of High-Quality and Large-Area Perovskite Single Crystals," *Advanced Functional Materials* 32 (2022): 2112758, https://doi.org/10.1002/adfm.202112758.

52. C. Liu, R. Wang, J. Liu, et al., "High-Performance Self-Driven $MAPbI_3$-$MAPbBr_3$ Perovskite Single Crystal Heterojunction Photodetectors for Ultra-Sensitive Weak Light Imaging," *Advanced Optical Materials* 13 (2025): 2403123, https://doi.org/10.1002/adom.202403123.

53. H. Wei, D. DeSantis, W. Wei, et al., "Dopant Compensation in Alloyed $CH_3NH_3PbBr_{3-x}Cl_x$ Perovskite Single Crystals for Gamma-Ray Spectroscopy," *Nature Materials* 16 (2017): 826–833, https://doi.org/10.1038/nmat4927.

54. L. Yin, H. Wu, W. Pan, et al., "Controlled Cooling for Synthesis of $Cs_2AgBiBr_6$ Single Crystals and Its Application for X-Ray Detection," *Advanced Optical Materials* 7 (2019): 1900491, https://doi.org/10.1002/adom.201900491.

55. Y. Liu, X. Zheng, Y. Fang, et al., "Ligand Assisted Growth of Perovskite Single Crystals With Low Defect Density," *Nature Communications* 12 (2021): 1686, https://doi.org/10.1038/s41467-021-21934-6.

56. Y. Liu, Y. Zhang, X. Zhu, et al., "Triple-Cation and Mixed-Halide Perovskite Single Crystal for High-Performance X-Ray Imaging," *Advanced Materials* 33 (2021): 2006010, https://doi.org/10.1002/adma.202006010.

57. X. Wang, Y. Xu, Y. Pan, et al., "Low-Noise X-Ray PIN Photodiodes Made of Perovskite Single Crystals by Solution-Processed Dopant Incorporated Epitaxial Growth," *Nano Energy* 89 (2021): 106311, https://doi.org/10.1016/j.nanoen.2021.106311.

58. H. Zhang, F. Wang, Y. Lu, et al., "High-Sensitivity X-Ray Detectors Based on Solution-Grown Caesium Lead Bromide Single Crystals," *Journal of Materials Chemistry C* 8 (2020): 1248–1256, https://doi.org/10.1039/C9TC05490A.

59. P. Zhang, Y. Hua, Y. Xu, et al., "Ultrasensitive and Robust 120 keV Hard X-Ray Imaging Detector Based on Mixed-Halide Perovskite $CsPbBr_{3-n}I_n$ Single Crystals," *Advanced Materials* 34 (2022): 2106562, https://doi.org/10.1002/adma.202106562.

60. H. Li, J. Song, W. Pan, et al., "Sensitive and Stable 2D Perovskite Single-Crystal X-Ray Detectors Enabled by a Supramolecular Anchor," *Advanced Materials* 32 (2020): 2003790, https://doi.org/10.1002/adma.202003790.

61. X. Zhang, D. Chu, B. Jia, et al., "Heterointerface Design of Perovskite Single Crystals for High-Performance X-Ray Imaging," *Advanced Materials* 36 (2024): 2305513, https://doi.org/10.1002/adma.202305513.

62. F. Cui, P. Zhang, L. Zhang, et al., "Liquid-Phase Epitaxial Growth of Large-Area $MAPbBr_{3-n}Cl_n$/$CsPbBr_3$ Perovskite Single-Crystal Heterojunction for Enhancing Sensitivity and Stability of X-Ray Detector," *Chemistry of Materials* 34 (2022): 9601–9612, https://doi.org/10.1021/acs.chemmater.2c02266.

63. W. Wei, Y. Zhang, Q. Xu, et al., "Monolithic Integration of Hybrid Perovskite Single Crystals With Heterogenous Substrate for Highly Sensitive X-Ray Imaging," *Nature Photonics* 11 (2017): 315–321, https://doi.org/10.1038/nphoton.2017.43.

64. L. Xue, Y. Du, Y. Li, et al., "Suppression of Ion Migration With a Composite Polymer Film in Perovskite Single-Crystal Photodetectors for Sensitive and Stable X-Ray Imaging," *Laser & Photonics Reviews* 20 (2026): 01802.

65. Z. Duan, K. Wang, H. Liu, et al., "Overcoming Solubility Limitations in Inverse Temperature Crystallization for Universal Growth of High-Quality Perovskite Single Crystals for X-Ray Detection," *Advanced Functional Materials* 36 (2026): 15287, https://doi.org/10.1002/adfm.202515287.

66. Q. Fan, H. Xu, Z.-K. Zhu, et al., "3D Lead-Free Double Perovskite via Anchoring a-Site Cation for Ultralow Dose and Stable X-Ray Detection," *Advanced Functional Materials* 35 (2025): 2505546, https://doi.org/10.1002/adfm.202505546.

67. M. J. Frisch, G. W. Trucks, and H. B. Schlegel, *Gaussian 16 A.03* (Gaussian, Inc., 2016).

68. T. D. Kühne, M. Iannuzzi, M. Del Ben, et al., "CP2K: an Electronic Structure and Molecular Dynamics Software Package-Quickstep: Efficient and Accurate Electronic Structure Calculations," *Journal of Chemical Physics* 152 (2020): 194103.

69. T. Lu and F. Chen, "Multiwfn: a Multifunctional Wavefunction Analyzer," *Journal of Computational Chemistry* 33 (2012): 580–592, https://doi.org/10.1002/jcc.22885.

70. J. Zhang and T. Lu, "Efficient Evaluation of Electrostatic Potential With Computerized Optimized Code," *Physical Chemistry Chemical Physics* 23 (2021): 20323–20328, https://doi.org/10.1039/D1CP02805G.

71. W. Humphrey, A. Dalke, and K. Schulten, "VMD: Visual Molecular Dynamics," *Journal of Molecular Graphics* 14 (1996): 33–38, https://doi.org/10.1016/0263-7855(96)00018-5.

72. L. Johnson, C. Li, Z. Liu, et al., "The Role of LiO_2 Solubility in O_2 Reduction in Aprotic Solvents and Its Consequences for Li–O_2 Batteries," *Nature Chemistry* 6 (2014): 1091–1099, https://doi.org/10.1038/nchem.2101.

Supporting Information

Additional supporting information can be found online in the Supporting Information section.

Supporting File: adma74774-sup-0001-SuppMat.docx.